A&A 385, 743–760 (2002)
DOI: 10.1051/0004-6361:20020195

Astronomy & Astrophysics

Cosmic shear from STIS pure parallels⋆

II. Analysis

H. Hämmerle[1,2], J.-M. Miralles[1,3], P. Schneider[1,2], T. Erben[2,4,5], R. A. E. Fosbury[3], W. Freudling[3], N. Pirzkal[3], B. Jain[6], and S. D. M. White[2]

[1] Institut für Astrophysik und Extraterrestrische Forschung der Universität Bonn, Auf dem Hügel 71, 53121 Bonn, Germany
[2] Max-Planck-Institut für Astrophysik, Karl-Schwarzschild Str. 1, 85748 Garching, Germany
[3] ST-ECF, Karl-Schwarzschild Str. 2, 85748 Garching, Germany
[4] Institut d'Astrophysique de Paris, 98bis boulevard Arago, 75014 Paris, France
[5] Observatoire de Paris, DEMIRM 61, Avenue de l'Observatoire, 75014 Paris, France
[6] Departement of Physics and Astronomy, University of Pennsylvania 209 S. 33rd Street, Philadelphia, PA 19104, USA

Received 10 October 2001 / Accepted 31 January 2002

Abstract. We report on the marginal detection of cosmic shear on sub-arcmin scales with archive data from the STIS camera on board HST. For the measurement 121 galaxy fields with a field of view of $51'' \times 51''$ are used to obtain an rms cosmic shear of $\sim$4% with 1.5σ significance. This value is consistent with groundbased results obtained by other groups on larger scales, and with theoretical predictions for a standard ΛCDM cosmology. To show the suitability of STIS for weak shear measurements we carefully investigated the stability of the PSF. We demonstrate that small temporal changes do not affect the cosmic shear measurement by more than $\sim$10%. We also discuss the influence of various weighting and selection schemes for the galaxy ellipticities.

Key words. cosmology: theory, dark matter, gravitational lensing, large-scale structure of Universe

1. Introduction

The tidal gravitational field due to the inhomogeneous distribution of matter in the Universe causes the distortion of light bundles from distant sources. As a consequence, the observed images of these sources are deformed. This tidal distortion yields a small but observable imprint on the distribution of galaxy ellipticities, an effect called "cosmic shear". As pointed out by Blandford et al. (1991), Miralda-Escude (1991) and Kaiser (1992), the statistical properties of the shear field reflect the statistical properties of the (dark) matter distribution in the Universe. Refined theoretical predictions, accounting for the non-linear evolution of the large-scale structure (e.g. Jain & Seljak 1997; Bernardeau et al. 1997; Kaiser 1998; Schneider et al. 1998a) and numerical simulations based on N-body results for cosmic structure evolution (e.g., van Waerbeke et al. 1999; Jain et al. 2000) yield expected shear amplitudes of about one percent on scales of a few arcminutes, depending on cosmological parameters and, in particular, on the normalization of the dark matter power spectrum (for recent reviews on the topic, see Mellier 1999; Bartelmann & Schneider 2001).

Because of the small scale of this effect, investigating it observationally is challenging. Early attempts (e.g. Mould et al. 1994; Schneider et al. 1998b) where plagued by the small data sets. Furthermore, dedicated image analysis software was needed to correct for observational effects like atmospheric seeing, anisotropic PSFs etc. (e.g, Bonnet & Mellier 1995; Kaiser et al. 1995, hereafter referred to as KSB95; Luppino & Kaiser 1997).

In March 2000, four groups nearly simultaneously announced the detection of cosmic shear on angular scales between $\sim 1'$ and $\sim 10'$ (Bacon et al. 2000; Kaiser et al. 2002; van Waerbeke et al. 2000; Wittman et al. 2000). All four groups presented results from groundbased wide-field imaging observations, at the level expected from currently popular cosmological models; particularly noteworthy is the impressive agreement between the four independent

Send offprint requests to: H. Hämmerle,
e-mail: hanne@astro.uni-bonn.de

⋆ Based on observations made with the NASA/ESA *Hubble Space Telescope*, obtained at the Space Telescope Science Institute (STScI) and from the data archive at the STScI, which is operated by AURA, Inc., under NASA contract NAS 5-26555.

results. Maoli et al. (2001) measured cosmic shear on an angular scale of a few arcminutes, using a survey carried out with the VLT, and again found results in agreement with the others. Van Waerbeke et al. (2001) presented the currently most accurate cosmic shear measurement, based on about 6.5 square degrees of CFHT wide-field imaging data. With the precision of these measurements, interesting cosmological constraints can be obtained from these data.

To extend these results to smaller angular scales where the non-linear effects of structure formation are more pronounced, other observing strategies are preferable. The noise of cosmic shear measurements is due mainly to two sources: intrinsic ellipticity of the source galaxies, and sampling variance. The relative importance of these two noise terms depends on the angular scale (e.g., Kaiser 1998); for small-scale cosmic shear measurements, the intrinsic ellipticity becomes dominant. To reduce this noise contribution, one should strive for imaging data with a large number density of galaxies, i.e., very deep images.

On the other hand, fainter galaxies have a smaller angular extent. The observed images are affected by a PSF smearing which must be corrected. The smaller galaxies need larger corrections and, accordingly, the corresponding uncertainty is larger. This means that shear measurements with groundbased telescopes have a natural limit, taking deeper images will not provide a significant increase in the number density of galaxies which can be used for a shear analysis. To measure accurate shapes of very faint and small galaxy images, space-based observations are required.

The Hubble Space Telescope currently carries two optical cameras, WFPC2 and STIS. Data from both of these instruments can in principle be used to study cosmic shear. The advantage of WFPC2 is its larger field-of-view, whereas the STIS imager has higher throughput and smaller pixel size, which is better adapted to the diffraction limit of the HST. In addition, it is known from weak lensing studies of clusters with WFPC2 (e.g., Hoekstra et al. 1998) that the PSF shows relatively large anisotropies towards the edges of the three WFC-chips. In contrast to wide-field groundbased images, where the PSF anisotropy is measured from the stars on the same image for which the shear analysis is performed, such a procedure is impossible for HST images: the fields are too small to detect a sufficient number of stars to model the PSF anisotropy. Since there are also indications that the PSF in WFPC2 changes with time (Hoekstra et al. 1998), we dismissed the idea of cosmic shear measurements with WFPC2 (but see Rhodes et al. 2001). Instead, analysing early STIS images, we concluded that the PSF anisotropy was very small, and did not change significantly with time.

With the initiation of a public parallel program with STIS in June 1997, we decided to use these archival data for a cosmic shear study. The data set that we have analysed has been described in Pirzkal et al. (2001; hereafter Paper I); briefly, we have produced a set of 498 coadded frames, some of which contain many stars and thus can be used to investigate the PSF, whereas others are dominated by galaxies and can be used for the shear analysis (see Paper I and Sect. 2 below for details).

The rest of the paper is organized as follows: in Sect. 2 we briefly describe our data set, the field selection and the data analysis. We devote Sect. 3 to a study of the PSF anisotropy, using images containing many stars, and demonstrate that the variations of the PSF anisotropy in time are indeed very small. A description of the cosmic shear analysis is given in Sect. 4, including our procedure for correcting for PSF anisotropy and smearing. We derive the maximum variations of the resulting mean shear per galaxy field when using the PSFs obtained from different star fields, and conclude that the STIS PSF anisotropy will not affect a cosmic shear measurement above the $\sim$10% level. Results are presented in Sect. 5. We obtain a $\sim 1.5\sigma$ detection of the rms shear on the scale of the STIS fields, with $\sqrt{\langle \overline{\gamma}^2 \rangle} = 3.87^{+1.29}_{-2.04}\%$. This value extends previous cosmic shear measurements to smaller angular scales. The influence of various weighting and selection schemes for the galaxy ellipticities is studied; in particular, we show that using different PSF anisotropy functions for the ellipticity corrections leaves the result basically unchanged. We tested our scheme with simulations and verified that it is able to recover a cosmic shear variance to within $\sim$15% of the input value. We conclude in Sect. 6 with a discussion of our results and an outlook on the currently running Pure Parallel GO Program with STIS.

2. Catalogue production and field selection

A preselection of the 498 associations defined in Paper I was done based on a visual inspection of the fields. We rejected fields in which the individual exposures were unsuitable for our project; reasons to not use a field were: bright stars and/or too many stars with diffraction spikes, (almost) empty fields (less than 5 objects per field), lower image quality than the rest of the images, or failure to converge of the iterative co-addition procedure described in Paper I. Some examples of fields which were rejected are shown in Fig. 1.

Furthermore we did not use more than one association (data taken in a single visit) at a particular pointing, selecting the one with the highest S/N. We only coadded images taken during the same visit for which the same guide stars were used so that we could verify that no rotation exists between successive images. These fields were used, however, to test the consistency of the shape measurement, see Sect. 4.3.

The fields were analysed using both SExtractor (Bertin & Arnouts 1996) and a modified version of the IMCAT package (KSB95; Erben et al. 2001) using the following procedure:

1. SExtractor catalogues were produced using the parameter file described in Sect. 5.2 of Paper I (see also: `http://www.stecf.org/projects/shear/`). In order

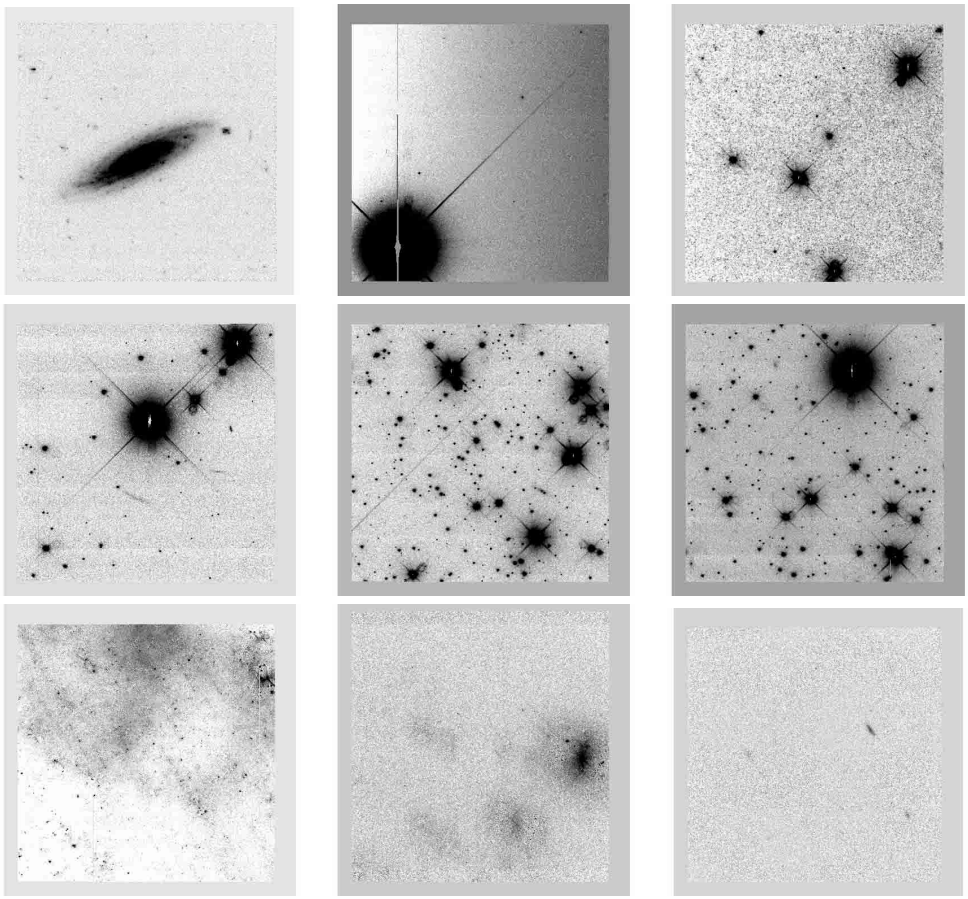

Fig. 1. Some examples of fields which were rejected after a visual inspection: the fields in the top row are dominated by one or a few big objects and are otherwise almost empty. In the star fields in the middle row there are many stars with diffraction spikes. The last row shows images with bad noise properties and one empty field.

to select well-measurable objects in the catalogues produced by SExtractor, we applied a "flag selection", disregarding all objects which were flagged internally by SExtractor due to problematic deblending and/or thresholding. Furthermore, we did a visual inspection of all the fields, masking suspect sources like galaxies with clearly separated sub-components and bright stars with diffraction spikes and ghosts.

2. IMCAT catalogues were produced simultaneously. Since IMCAT was developed specifically for shape measurements but not for a reliable detection of sources, we performed a "two-code selection": IMCAT and SExtractor catalogues were merged requiring an object to be detected uniquely by both codes, which means that no object had more than one counterpart in any of the two catalogues in a radius of 125 mas (5 subsampled STIS pixels) for the central coordinates. The number of objects in the merged catalogue diminishes by no more than 5 objects with respect to the SExtractor catalogue for the galaxy fields and includes 98% of objects for the star fields. The objects which were rejected were either flagged by IMCAT (near the border, negative flux or half-light radii) or there were multiple detections by IMCAT where there was only one in SExtractor, which is typical for galaxies with resolved star forming regions.
3. In the final merged catalogue we used size and shape parameters from IMCAT, since it was designed specifically to measure robust ellipticities for faint galaxy images and allows for the correction of measured image ellipticities for shape distortion introduced by the PSF (Luppino & Kaiser 1997; Hoekstra et al. 1998). The position and magnitude were estimated with SExtractor where we used MAG_ZP = 26.38 which is the AB magnitude zeropoint for the STIS CLEAR filter mode. The objects retained typically have a S/N of more than 5. The signal-to-noise ratio is measured with the `snratio` parameter of IMCAT (see Erben et al. 2001).

After catalogue production, we rejected fields with fewer than 10 (100) objects for galaxy (star) fields, which leaves us with 121 and 51 fields, respectively.

To select stars, we used size vs. S/N plots in which the stars populate a well-defined strip, as can be seen for two examples of star fields in Fig. 2. Since the images have very different exposure times, we decided to use S/N rather than magnitude to be able to use common criteria for all fields. For the rest of the paper we assume that stars

have $2.1 < r_{\rm h} < 2.6$ in subsampled STIS pixels (52 mas $< r_{\rm h} <$ 65 mas) and $S/N > 10$; galaxies are selected with $r_{\rm h} > 2.6$. The half-light radius is measured with IMCAT and is the radius at which half of the flux of an object is included.

The mean number of selected galaxies per association is 18 on the galaxy fields (25/arcmin^2), which is similar to the galaxy number density found by Rhodes et al. (2001) in the "Groth Strip" with $I < 26$ mag; however, the way galaxies are selected in their paper is different from ours.

3. Analysis of PSF anisotropy

Our main scientific motivation for using data from the STIS Parallel Survey is their suitability for the detection and measurement of cosmic shear. Since the expected distortion of image ellipticities on the STIS angular scale is a few percent, any instrumental distortion and other causes of PSF anisotropy need to be understood and controlled to an accuracy of $\lesssim$1%. In particular, the PSF anisotropy needs to be either small in amplitude or stable in time.

The shape of the PSF anisotropy is estimated using the KSB95 ellipticity parameters. These describe the elongation and orientation of the equivalent ellipse which best reproduces the PSF shape, as determined from the weighted second order brightness moments,

$$Q_{ij} = \int \mathrm{d}^2\theta\, W(\theta)\theta_i\theta_j f(\boldsymbol{\theta}), \tag{1}$$

where $\boldsymbol{\theta} = (\theta_1, \theta_2)$, $\theta = |\boldsymbol{\theta}|$, and angles are measured relative to the centroid $\boldsymbol{\theta_{\rm c}}$ of the object, as defined by

$$\int \mathrm{d}^2\theta\, W(\theta_{\rm c})\theta_i f(\boldsymbol{\theta_{\rm c}}) = 0. \tag{2}$$

$f(\boldsymbol{\theta})$ is the observed surface brightness and $W(\theta)$ is a weight function, which we take to be a Gaussian with an appropriate filter scale. This scale is obtained by determining the significance of detecting a peak for a range of filter scales and using the scale which gives maximum significance as described in KSB95.

The complex ellipticities are then defined as

$$e = \frac{Q_{11} - Q_{22} + 2\mathrm{i}Q_{12}}{Q_{11} + Q_{22}}; \tag{3}$$

for an object with elliptical isophotes

$$e = \frac{1 - r^2}{1 + r^2}\, \mathrm{e}^{2\mathrm{i}\vartheta} \tag{4}$$

where $r = b/a$ is the axis ratio of the corresponding ellipse and its position angle is $\vartheta = 0.5 \arctan e_2/e_1$.

In Fig. 3 the mean values of the two ellipticity components of stars over the whole field are shown as a function of the exposure date. The mean ellipticity of all fields is 1.5% for e_1 and 0.5% for e_2 with a dispersion of 1%, which is sufficiently small for our cosmic shear analysis, as will be shown in Sects. 4.2 and 5.3. Only a small fraction of the scatter is due to the different distribution of stars over the fields. If we divide the star fields into time intervals, the mean ellipticities agree with each other on the 1σ level, therefore the anisotropy can be considered to be constant over the time period covered.

In addition to the variation from field to field (i.e., in time), we also find a spatial variation of the PSF within individual fields. This effect is shown for two fields in Figs. 4 and 5, bottom left panels. We fit the ellipticities with a second order polynomial at the position $\boldsymbol{\theta} = (x, y)$ on the CCD:

$$e_\alpha(\boldsymbol{\theta}) = a_{\alpha 0} + a_{\alpha 1}x + a_{\alpha 2}x^2 + a_{\alpha 3}y + a_{\alpha 4}y^2 + a_{\alpha 5}xy, \tag{5}$$

where $\alpha = 1, 2$. For the fitting an iterative procedure was used: for stars selected by $r_{\rm h}$ and S/N, as described in Sect. 2, a first guess of the polynomial was calculated by solving the normal equations. From this initial fit, a dispersion was calculated by

$$\sigma_\alpha^2 = \frac{\sum_i (e_\alpha(\theta_i) - e_{\alpha i})^2}{N_{\rm star} - N_{\rm coeff}}. \tag{6}$$

Only stars for which the ellipticity components did not deviate more than 3σ in both e_1 and e_2 from the first fit were used for the second fit. The 3σ clipping was then applied to all the preselected stars (not only the left-overs from the first fit) to avoid biasing. This procedure was repeated until it converged, which was typically after no more than 10 iterations, with 5–10% outliers disregarded. For the two star fields in Fig. 2, the ellipticities and the values for the fitted polynomials at the star positions are shown in Figs. 4 and 5.

For the anisotropy correction of the galaxies each star field polynomial is applied to each galaxy field (see Sect. 4.2). The time period when the galaxy fields were observed is well covered by the observation times of the star fields.

To check the stability of our coaddition procedure, we also analysed individual exposures with respect to PSF size and anisotropy. The stars in the individual exposures were selected by $1.1 < r_{\rm h} < 1.4$ STIS pixels and $S/N > 10$. We find that the stars in the drizzled images are slightly larger ($\approx$0.1 subsampled STIS pixels) than in the individual exposures (see Table 1). The broadening of the PSF is a known property of drizzle if one uses PIXFRAC = 1 (see Fruchter & Hook 1998). In Sect. 5.4 we describe some simulations carried out to check our analysis of the cosmic shear; in the simulated star fields we find the same increase in sizes of stars ($\approx$5%) from the individual images to the drizzled ones, as we observed in the archive data.

From the results in Table 1 we find more stars in the drizzled images than in the undrizzled ones. For associations where many individual exposures have been coadded this can be naturally attributed to a gain in S/N. However, we also find more objects if just one individual image is drizzled, as can be seen in the last two rows of Table 1 for the star field o4xcll010_1_ass. This is a result of the combination of drizzling and IMCAT: an object

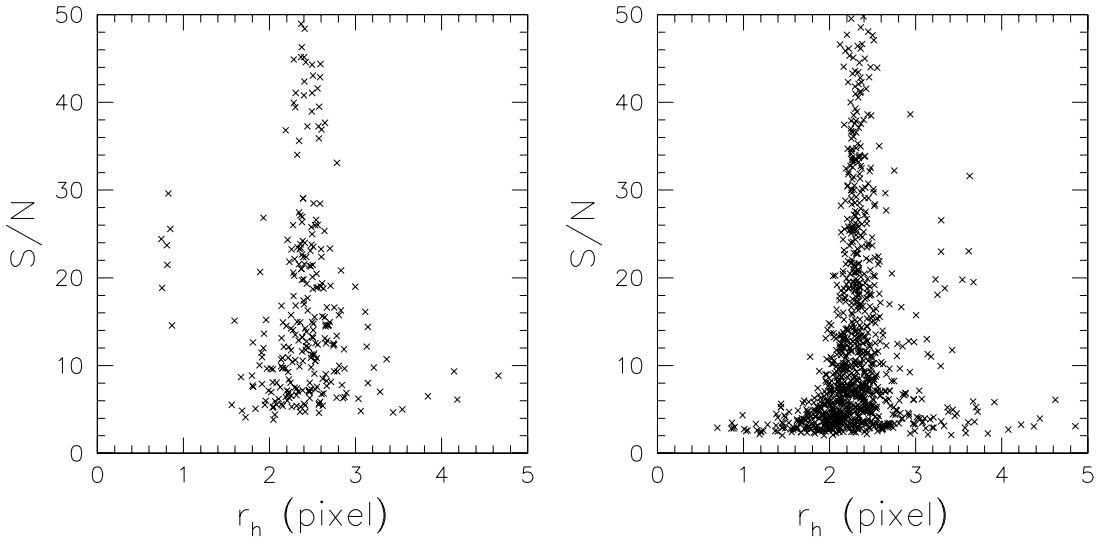

Fig. 2. Size vs. S/N diagrams for the star fields o3zf01010_3_ass (left) and o48b41010_3_ass (right). The half-light radius r_h is given in subsampled STIS pixels. One can clearly distinguish the strip populated by stars around $r_\mathrm{h} = 2.3$ (57.5 mas). The strip at ≈0.8 pixels seen in the left panel is due to single noisy pixels (see also Fig. 6 of Paper I).

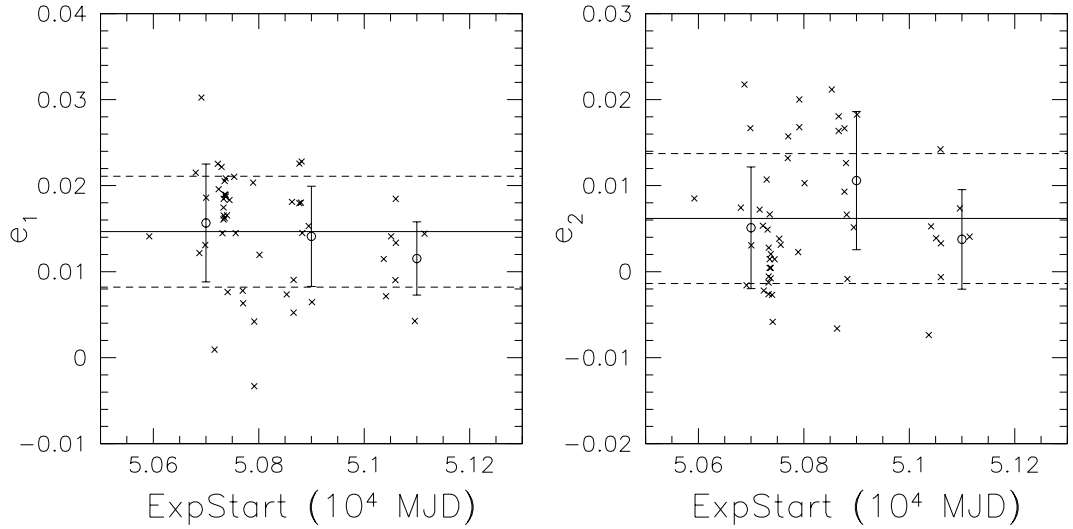

Fig. 3. Mean of the ellipticity components e_1 (left) and e_2 (right) of the star fields vs. exposure start time (Modified Julian Date). The straight lines show the mean over all the fields, the dashed lines show the 1σ dispersion. The circles show the mean over stars in bins between 5.06×10^4, 5.08×10^4, 5.10×10^4, 5.12×10^4 (MJD) with the error bars showing the 1σ dispersion.

which has a size of only one STIS pixel or slightly larger is distributed over more subsampled STIS pixels in the drizzling process. Therefore an object which was rejected by IMCAT on the undrizzled image because of its size of only ≈1 pixel (and therefore high probability to be noise) is now detected significantly.

For the individual undrizzled images of some of the star fields, we also analysed the PSF anisotropy and we find very short timescale variations of the anisotropy pattern over the fields, as can be seen in Fig. 6 for two individual exposures of the star field o3zf01010_3_ass. The short timescale variations of the PSF anisotropy pattern are likely to be due to "breathing" of the telescope. However, they do not affect our analysis, as will be shown in Sect. 4.2.

4. Shear analysis

4.1. Cosmic shear theory

The rms shear in a circular aperture with angular radius θ is related to the power spectrum of the surface mass density κ by

$$\langle \overline{\gamma}^2 \rangle = 2\pi \int_0^\infty \mathrm{d}s\, s\, P_\kappa(s)\, [I(s\theta)]^2\,, \tag{7}$$

where $I(\eta) := J_1(\eta)/(\pi\eta)$ and J_1 is the Bessel function of the first kind. P_κ is in turn related to the three-dimensional power spectrum by a simple projection (see e.g. Blandford et al. 1991; Kaiser 1992; Schneider et al. 1998a; Mellier 1999; Bartelmann & Schneider 2001). A similar formula for a square aperture is given by Kaiser (1992).

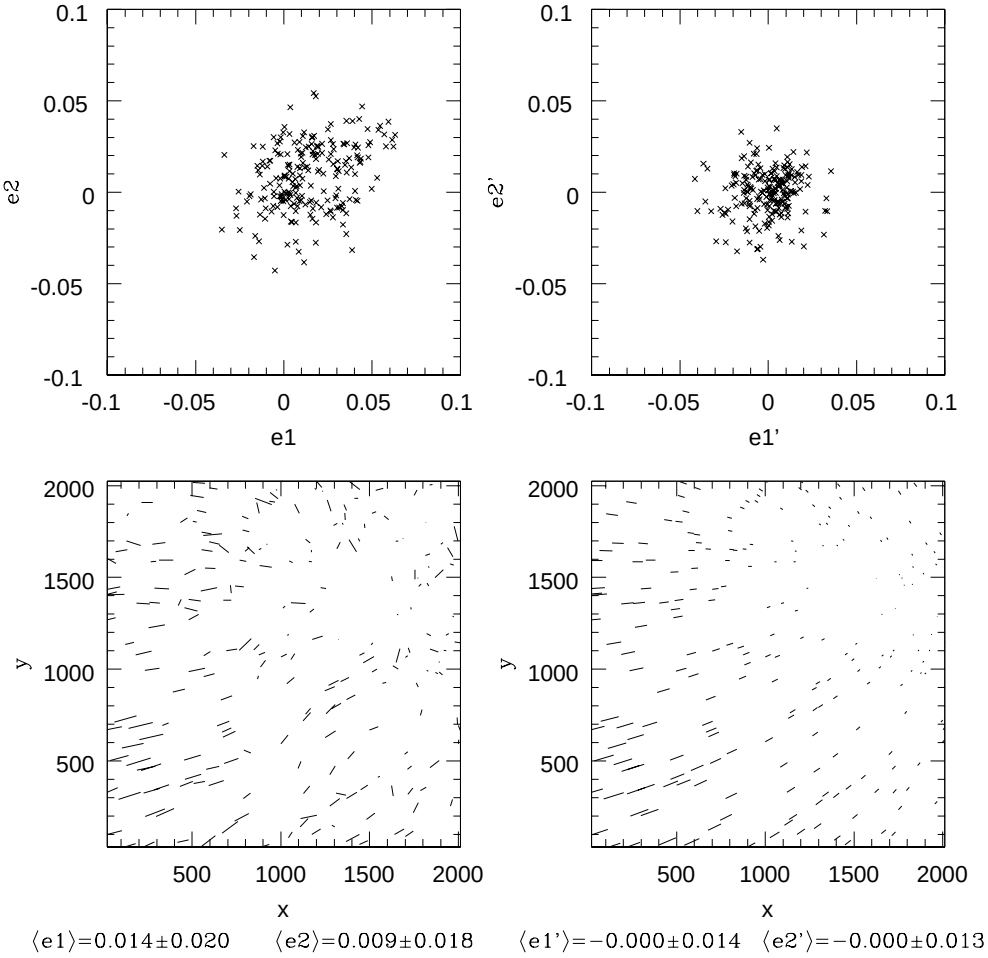

Fig. 4. For the star field o3zf01010_3_ass the distribution of the ellipticities of stars are shown before (top left) and after (top right) correcting for PSF anisotropy. The bottom left panel shows the spatial distribution of the ellipticities across the STIS field, the bottom right the fitted second-order polynomial at the star positions. The length of the sticks indicates the modulus of the ellipticity, the orientation gives the position angle. The mean ellipticities before and after the correction are given at the bottom. Note that the mean ellipticity after the correction is zero and that the dispersion decreases.

Equation (7) is correct if one measures the shear in a circular aperture. To quickly compare our result from the square STIS field to theoretical predictions, we calculate the theoretically expected value for a circular field with the same area, which would then have an effective radius of about $30''$. The error from this approximation is much smaller than the statistical error bars on our present result.

Let e_{in} denote the complex ellipticity of the ith galaxy on the nth field, then the quantity we measure for each field is

$$\overline{\gamma}_n^2 := \frac{1}{N_n(N_n-1)} \sum_{i\neq j} e_{in} e_{jn}^\star \tag{8}$$

where N_n is the number of galaxies in the nth field, or

$$\overline{\gamma}_n^2 := \frac{\sum_{i\neq j} w_{in} w_{jn} e_{in} e_{jn}^\star}{\sum_{i\neq j} w_{in} w_{jn}}, \tag{9}$$

where w_{in} is the weight of the ith galaxy in the nth field, and $e^\star$ denotes the complex conjugate. This is an unbiased estimate of the cosmic shear dispersion in the nth field. (Note that $\overline{\gamma}_n^2$ is not positive definite.) From this, one obtains an unbiased estimate of the cosmic shear dispersion:

$$\left\langle \overline{\gamma}^2 \right\rangle = \frac{1}{N_\mathrm{f}} \sum_{n=1}^{N_\mathrm{f}} \overline{\gamma}_n^2, \tag{10}$$

where N_f is the number of galaxy fields, or

$$\left\langle \overline{\gamma}^2 \right\rangle = \frac{\sum N_n \overline{\gamma}_n^2}{\sum N_n}, \tag{11}$$

where we weight each field by the number of galaxies per field to minimize Poisson noise. Since our galaxy fields have a large spread in exposure times, and therefore in number of galaxies per field, we use Eq. (11) for our analysis.

Assuming N_f galaxy fields with the same number $N_n = N$ of galaxies per field and the same redshift distribution of the sources, the errors from the intrinsic

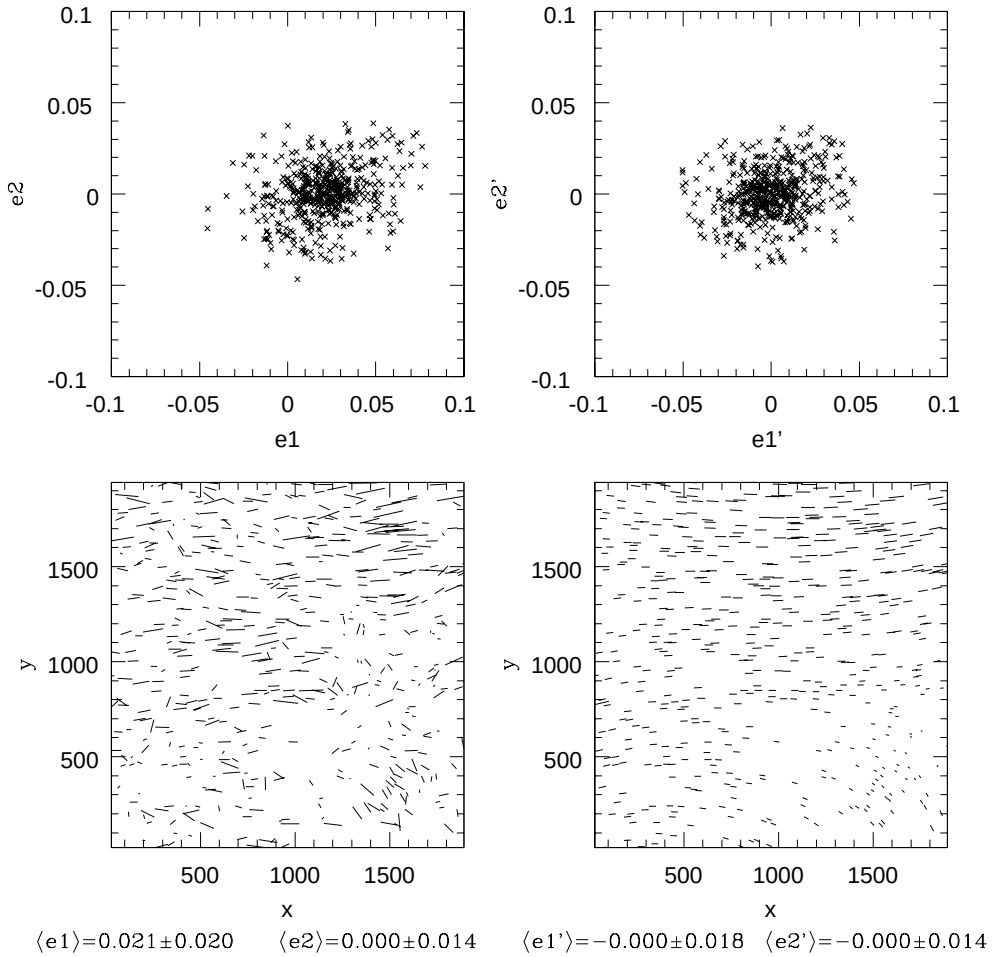

Fig. 5. Same as Fig. 4 for the star field o48b41010_3_ass.

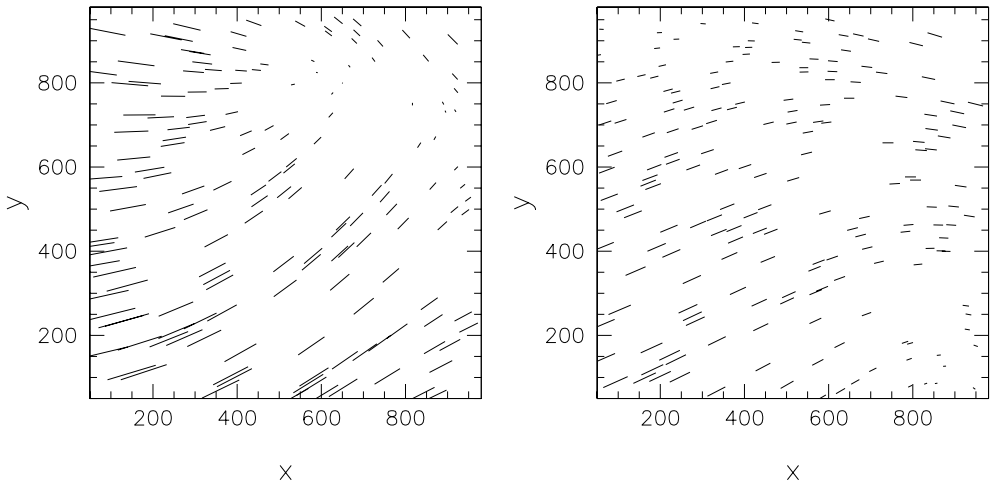

Fig. 6. We show the values of the polynomials for the anisotropy correction of the two individual (undrizzled) exposures o3zf01040 (left) and o3zf01090 (right) which are members of the association o3zf01010_3_ass shown in Fig. 4. The two individual fields were taken with a time difference of only 30 minutes and demonstrate the very short timescale variations of the PSF anisotropy pattern.

ellipticity distribution and the cosmic variance in the absence of kurtosis are given by

$$\sigma^2_{\rm intr} = \sqrt{2}\frac{\sigma^2_{\rm s}}{N\sqrt{N_{\rm f}}} \tag{12}$$

and

$$\sigma^2_{\rm cv} = \sqrt{2}\left\langle\overline{\gamma}^2\right\rangle/\sqrt{N_{\rm f}}. \tag{13}$$

With an rms intrinsic ellipticity $\sigma_{\rm s} \approx \sqrt{2}\times 26\%$ (see Fig. 11) and an expected shear of a few percent on the

Table 1. Mean half-light radius and error on the mean for individual exposures (in STIS pixels) and for the *corresponding coadded association (in subsampled STIS pixels)* for all stars on an image. The first column identifies the individual exposure or the coadded image. The second column yields the number of stars used to calculate the mean. The third and fourth columns show the mean half-light radius and the error on the mean for individual exposures in STIS pixels (50 mas) and for the coadded images in subsampled STIS pixels (25 mas). The last two columns show the date of observation $t_{\rm date}$ (MJD) and the exposure time $t_{\rm exp}$ in "s".

image	N	$\langle r_{\rm h}\rangle$ image pixels	σ $\times 10^3$	$t_{\rm date}$ (MJD) 50000+	$t_{\rm exp}$ s
o3zf01010	132	1.1503	6.8	592.4319	60
o3zf01020	139	1.1563	6.9	592.4344	60
o3zf01030	135	1.1389	6.4	592.4369	60
o3zf01040	132	1.1296	5.9	592.4415	60
o3zf01090	148	1.1021	5.2	592.4592	64
o3zf010a0	158	1.0989	5.2	592.4634	72
o3zf010b0	151	1.1505	6.0	592.5012	72
o3zf010c0	158	1.1357	6.6	592.5039	72
o3zf010d0	147	1.1345	5.2	592.5087	72
o3zf010e0	155	1.1219	5.8	592.5114	72
o3zf010f0	151	1.1227	5.7	592.5166	72
o3zf010g0	147	1.1040	5.0	592.5192	72
o3zf01010_3	*322*	*2.4016*	*6.3*	*592.4319*	*808*
o48b3w010	435	1.1142	3.9	735.3806	400
o48b51010	430	1.1237	4.1	737.1772	400
o48b5d010	420	1.1129	3.8	737.3673	400
o48b5p010	397	1.1044	4.2	737.6852	400
o48b3w010_3	*660*	*2.3397*	*4.6*	*735.3806*	*1600*
o4xcll010	432	1.1631	3.3	1096.1600	300
o4xcll010_1	*467*	*2.4238*	*5.8*	*1096.1600*	*300*

STIS angular scale we find $\sigma^2_{\rm intr} \approx 10^{-3}$ and $\sigma^2_{\rm cv} \approx 10^{-4}$, showing that the noise from the intrinsic ellipticity distribution dominates over the sampling variance.

4.2. Anisotropy correction

As shown in Sect. 3, the STIS PSF is remarkably symmetric, i.e., it exhibits a very small ($\lesssim$1%) anisotropy component. Furthermore, it does not vary significantly in time ($\sigma \approx 1\%$), as shown in Fig. 3.

Of the 51 star fields, 21 were selected for having a good spatial coverage and a small intrinsic dispersion in the ellipticities of stars, which allowed us to obtain good fits to the anisotropy pattern, to minimize the noise in the PSF correction.

The galaxy ellipticities were corrected for PSF anisotropy according to KSB95 as follows:

The total response of a galaxy ellipticity to a shear and the PSF is given by

$$e - e_{\rm s} = P^\gamma \gamma + P_{\rm sm} q^*; \tag{14}$$

where e and $e_{\rm s}$ are the observed and intrinsic ellipticities, respectively, and

$$P^\gamma = P_{\rm sh} - \left(\frac{P_{\rm sh}}{P_{\rm sm}}\right)^* P_{\rm sm}, \tag{15}$$

where the tensors $P_{\rm sh}$ and $P_{\rm sm}$ can be calculated from the galaxy light profile with the same filter scale of the galaxy as for the weight function in Eq. (1); see KSB95. The ratio $(P_{\rm sh}/P_{\rm sm})^* \equiv ({\rm tr}P^*_{\rm sh}/{\rm tr}P^*_{\rm sm})$ is calculated from stars with the filter scale of the galaxy. The second term in Eq. (15) accounts for the circular smearing of the isotropic part of the PSF. The stellar anisotropy kernel q^* which is needed to correct for PSF anisotropy can be calculated by noting that for stars $e^*_{\rm s} = 0$ and $\gamma^* = 0$, so that

$$q^* = (P^*_{\rm sm})^{-1} e^*. \tag{16}$$

The anisotropy-corrected ellipticity is then calculated by

$$e^{\rm ani} = e - P_{\rm sm} q^*. \tag{17}$$

In Fig. 7 we show for one galaxy field the uncorrected ellipticities of the galaxies in the left panel and the mean of the anisotropy-corrected ellipticities over all galaxies in the field when correcting with different star field polynomials in the right panel. There is a shift in the negative e_1 direction compared to the mean uncorrected ellipticity, as is expected (see Sect. 3). The dispersion between different corrections is much less than 1% which shows that variations of the PSF anisotropy are small.

In Fig. 8 the mean ellipticity for all the galaxy fields is shown with and without the PSF anisotropy correction. It illustrates that the PSF anisotropy correction changes the mean ellipticity by an amount typically smaller than 1%. Also, the dispersion between different PSF models from different star fields is much less than 1%, which means that the changes of the PSF anisotropy seen in different star fields are sufficiently small to allow us to use one (or a suitable combination) of them for the actual analysis.

The effect of PSF anisotropy corrections is considerably less than the expected cosmic shear signal, which confirms our expectation that the image quality of STIS is very well suited for our project. We also note that the mean PSF anisotropy correction points towards the negative e_1 direction, in agreement with the stellar ellipticity plotted in Fig. 3.

4.3. Smearing correction

The smearing corrected ellipticity of each galaxy is calculated by

$$e^{\rm iso} = (P^\gamma)^{-1} e^{\rm ani}, \tag{18}$$

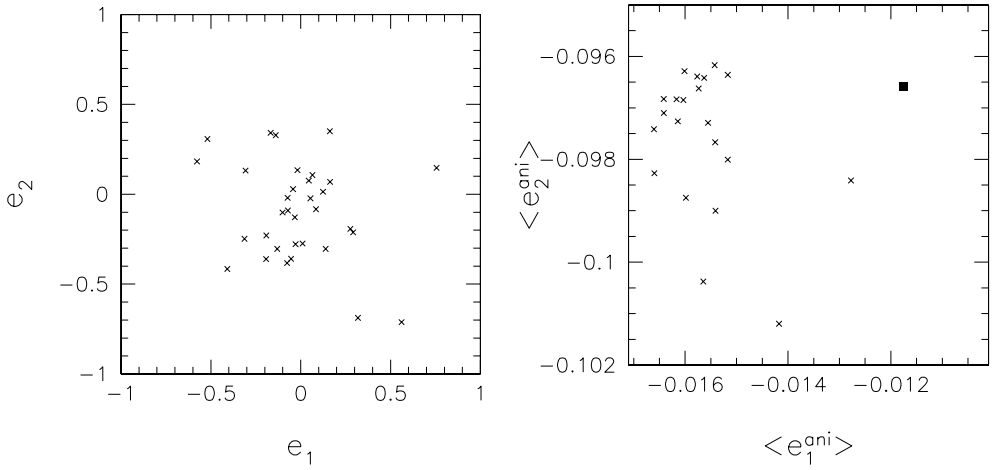

Fig. 7. For the galaxy field o46p02010_3_ass: in the left panel the uncorrected ellipticities of individual galaxies are shown, in the right panel the mean of the anisotropy-corrected ellipticity $\langle e^{\rm ani}\rangle$ over the galaxy field for corrections with different star fields; the square shows the mean over the uncorrected ellipticities. Note the different scalings of the panels.

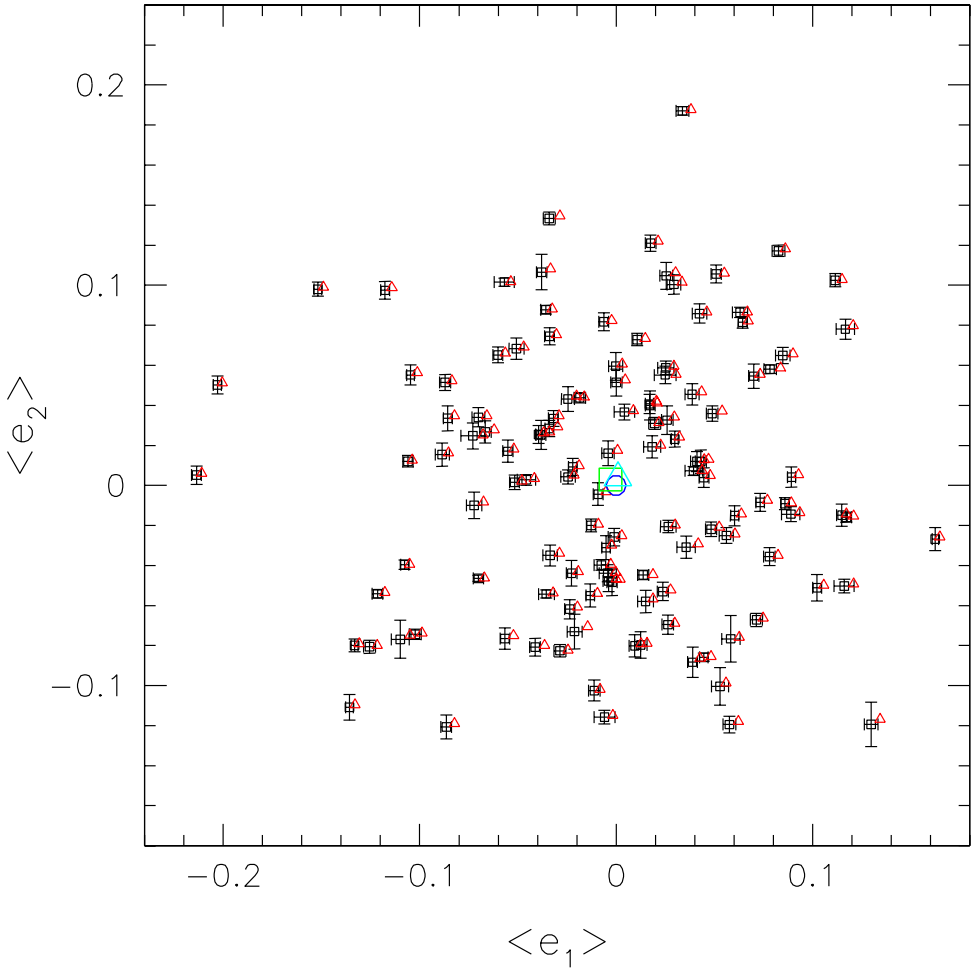

Fig. 8. For 121 galaxy fields we plot the mean uncorrected ellipticity of galaxies (triangles) as well as the mean anisotropy corrected ellipticity (squares). The error bars attached to the squares denote 3 times the dispersion of the field-averaged corrected ellipticities when the different PSF model fits are used; the error on the mean is much smaller than the symbols used. The shift of the corrected mean ellipticities towards negative e_1 is expected from the behaviour of the stellar ellipticities plotted in Fig. 3. The big triangle and big square in the centre denote the mean over all galaxy fields of the uncorrected and corrected mean ellipticities, respectively; the size of the symbols represent the 1σ errors on the mean. The circle shows the origin for reference. The mean shear is compatible with zero.

see Eqs. (14) and (17), which is an unbiased (provided that $\langle e_s \rangle = 0$) but very noisy estimate of the shear γ. We apply a scalar inversion of $(P^\gamma)^{-1} = 2/\mathrm{tr}P^\gamma$ since it is less noisy than the full tensor inversion, as found by Erben et al. (2001).

To calculate P^γ (see Eq. (15)) for each galaxy, we need to estimate $(P_{\rm sh}/P_{\rm sm})^*$ from the light profile of the stars with the filter scale of the galaxy (see Eq. (1)). We find that $(P_{\rm sh}/P_{\rm sm})^*$ is spatially constant, as for most gound-based telescopes (Erben et al. 2001) and calculate the mean of this quantity over the stars in a given field for different filter scales. We find that $(P_{\rm sh}/P_{\rm sm})^*$ varies from star field to star field (i.e., in time), as does the PSF anisotropy. If we take the mean over the star fields for different filter scales, we find that $(P_{\rm sh}/P_{\rm sm})^*$ increases with filter scale and is constant for large objects (see Fig. 9). This behaviour is expected since small objects are typically more affected by smearing of the PSF and therefore have a larger $P^*_{\rm sm}$.

The error bars on $(P_{\rm sh}/P_{\rm sm})^*$ for different filter scales are due to a variation in the size of the stars from field to field, as is shown in Fig. 10, where we plot the mean half-light radius of all the stars in a star field vs. the time when the field was observed. The mean size of stars varies by about 0.2 subsampled STIS pixels. We find that in fields with larger mean half-light radius, $(P_{\rm sh}/P_{\rm sm})^*$ is bigger for all filter scales, i.e., the smearing correction is larger. The increasing error bars for larger filter scale are due to the fact that stars are small ($\approx$2.3 subsampled STIS pixels) and therefore we detect more and more (background) noise if we go to larger filter scales.

Since for the smearing correction one has to divide by P^γ (see Eq. (18)), objects with small values of P^γ can get unphysically big ellipticities, which dominate the cosmic shear signal even after introducing a weighting of galaxies as shown in the following section. We therefore decide to introduce a cut in P^γ in addition to the weighting, requiring that "good" galaxies should have $\sqrt{\det P^\gamma} \geq 0.2$ (in short: $P^\gamma > 0.2$). The effect of different cuts in P^γ on the cosmic shear measurement is discussed in Sect. 5.2.

In Fig. 11 we show the probability distribution of the fully corrected ellipticities for all galaxies with $P^\gamma > 0.2$ on all galaxy fields. The mean ellipticity is compatible with zero and the dispersion in both components is 26%. The dispersion is consistent with that found by Hudson et al. (1998), if one takes into account the different mean magnitude of the galaxies and the different pixel scale. The kurtosis is consistent with a Gaussian; the skewness is slightly larger than one would expect given the number of galaxies.

For the associations which were observed several times at different visits, we compared the catalogues of objects obtained from the different exposures and find that the number of reliable detections ($S/N > 2$) differs. Comparing the raw as well as the fully corrected ellipticities, we find that they agree very well regarding orientation angle and modulus of the ellipticity, with the exception of a few faint extended objects with low signal-to-noise ratio ($S/N < 10$).

4.4. Weighting scheme

The PSF correction we apply to the galaxy ellipticities amplifies the errors in the measurement, which can eventually produce unphysical ellipticities much larger than unity, as noted in the previous section. For weak shear the ensemble of corrected ellipticities measured is the best estimate one has of the intrinsic (unlensed) ellipticity distribution. But this distribution is broadened and the high ellipticity tail is more pronounced because of the noise amplification. With the weighting scheme we want to minimize the influence of objects with high ellipticities which most probably originate from noise.

Our expectation is that objects which are small and/or have low S/N ar most affected by noise. For each galaxy we search for the 20 next neighbours in a two dimensional parameter space of half-light radius and signal-to-noise ratio (see Erben et al. 2001) containing all galaxies from all galaxy fields. Since the average number density on our galaxy fields is only 18, we have to put all galaxies together in one catalogue to do the next neighbour search. For the STIS images the galaxies have very similar properties in the chosen parameter space, therefore combining them in one catalogue is maintainable.

Since the scalings in $r_{\rm h}$ and S/N are very different we transform the coordinate axes in the following way: we sort the objects in ascending order in both coordinates separately and assign the running number as the new coordinate. The 20 next neighbours are then found in this new parameter space. For each galaxy we calculate the ellipticity dispersion from the M next neighbours

$$\sigma^2_{\rm NN} = \frac{1}{M-1} \sum_{i=1}^{M} \left(e_i^2 - \langle e \rangle^2 \right), \tag{19}$$

which we assign as the measurement error to the galaxy. The weights for the galaxies are obtained by a simple $w_{\rm NN} = 1/\sigma^2_{\rm NN}$ weighting

The dispersion $\sigma_{\rm NN}$ and the corresponding weights $w_{\rm NN}$ are shown in Fig. 12. The correlations seen in the plot are due to objects with similar properties, e.g. at $r_{\rm h} \approx 7$ there are several elliptical galaxies with a compact, bright centre.

5. Results

5.1. Estimation of the cosmic shear

The procedure to estimate the cosmic shear is the following:

PSF correction: The raw ellipticities of the galaxies are corrected for PSF anisotropy with the polynomials from the 21 star fields. For each of the star fields we also calculate $(P_{\rm sh}/P_{\rm sm})^*$ for different filter scales and from that

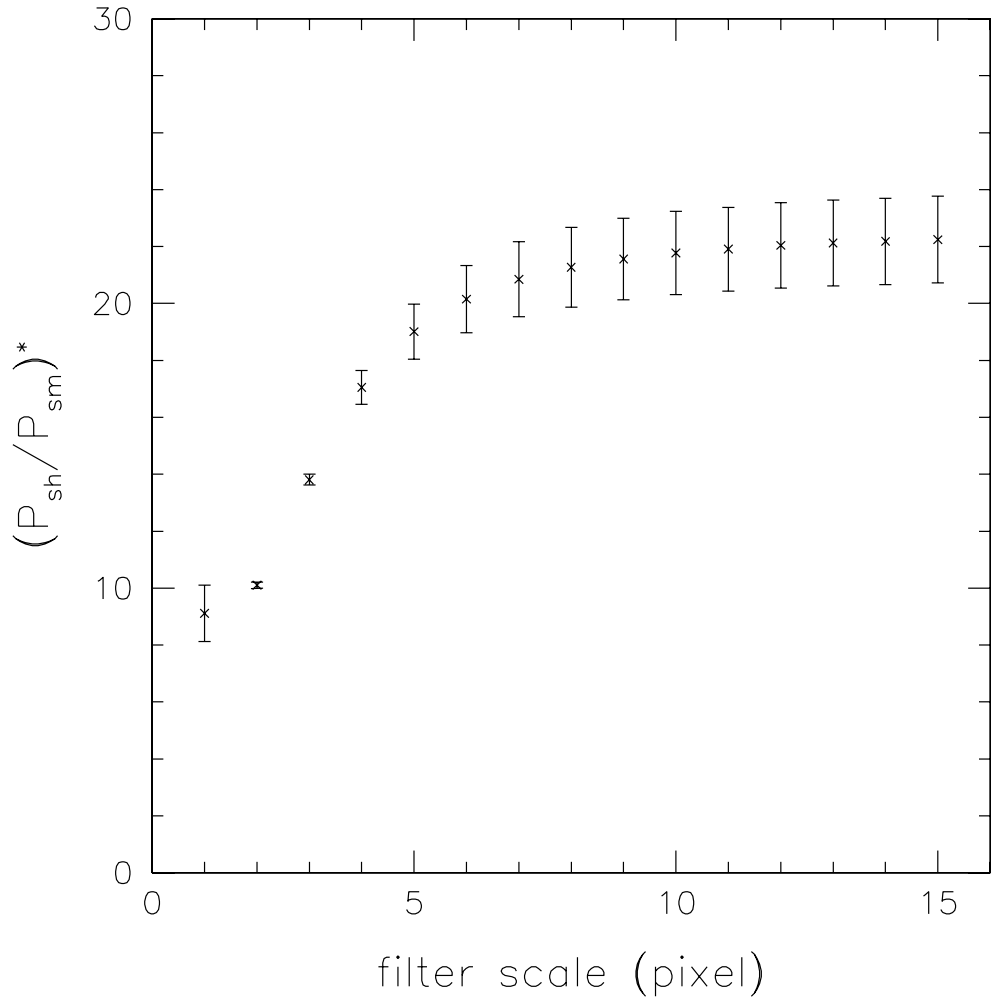

Fig. 9. The mean of $(P_{\rm sh}/P_{\rm sm})^*$ over all stars which were used for the anisotropy correction is shown for different filter scales. The error bars show the dispersion between different star fields.

P^γ for the filter scale of the galaxy. For each galaxy we then have 21 anisotropy corrected ellipticities and 21 smearing corrected tensors P^γ. The mean correction is obtained by then averaging over the star fields. From the mean anisotropy-corrected ellipticities and the mean P^γ for each galaxy we calculate the fully corrected ellipticity (see Eq. (18)).

Cosmic Shear: The fully corrected ellipticity is an unbiased (although very noisy) estimate of the shear. Therefore, we use it to calculate the cosmic shear estimator for each galaxy field, given in Eqs. (8) and (9). By taking the average over all the galaxy fields as in Eq. (11) we obtain the measured cosmic shear value in our data. The error on the cosmic shear result is calculated as the statistical error on the mean, which for a weighted mean

$$\langle x\rangle = \frac{\sum_i w_i x_i}{\sum_i w_i} \tag{20}$$

is given by

$$\sigma^2_{\langle x\rangle} = \frac{\sum_i w_i^2}{\sum_i w_i \left(\left(\sum_i w_i\right)^2 - \sum_i w_i^2\right)} \sum_i w_i (x_i - \langle x\rangle)^2. \tag{21}$$

We also compute the confidence level of the results from the dispersion of the probability distribution of the cosmic shear estimator in Eq. (11) obtained by randomizing the galaxy orientations (Fig. 13). If we use all galaxy fields and weight individual galaxies according to $w_{\rm NN}$ we find in 2.9% of the randomizations a value higher than the actually measured one.

Our results for the cosmic shear and the corresponding errors (see Eq. (21)) are shown in Table 2 for all galaxy fields and for fields with more than 10 (15) galaxies per field. Note that in some of the fields there are fewer than 10 galaxies per field (but still more than 5), since we restrict our analysis to "good" galaxies, i.e., objects with $r_{\rm h} > 2.6$ subsampled STIS pixels (see Sect. 2) and $P^\gamma \geq 0.2$ (see Sect. 4.3). Using only fields with a higher number density of galaxies we find a larger cosmic shear signal, whereas the error stays more or less the same although we average over fewer galaxy fields, even if we do not apply any weighting to the galaxy fields.

We also investigated the behaviour of the cosmic shear estimator in bins of roughly equal number of fields for different number densities of galaxies and find

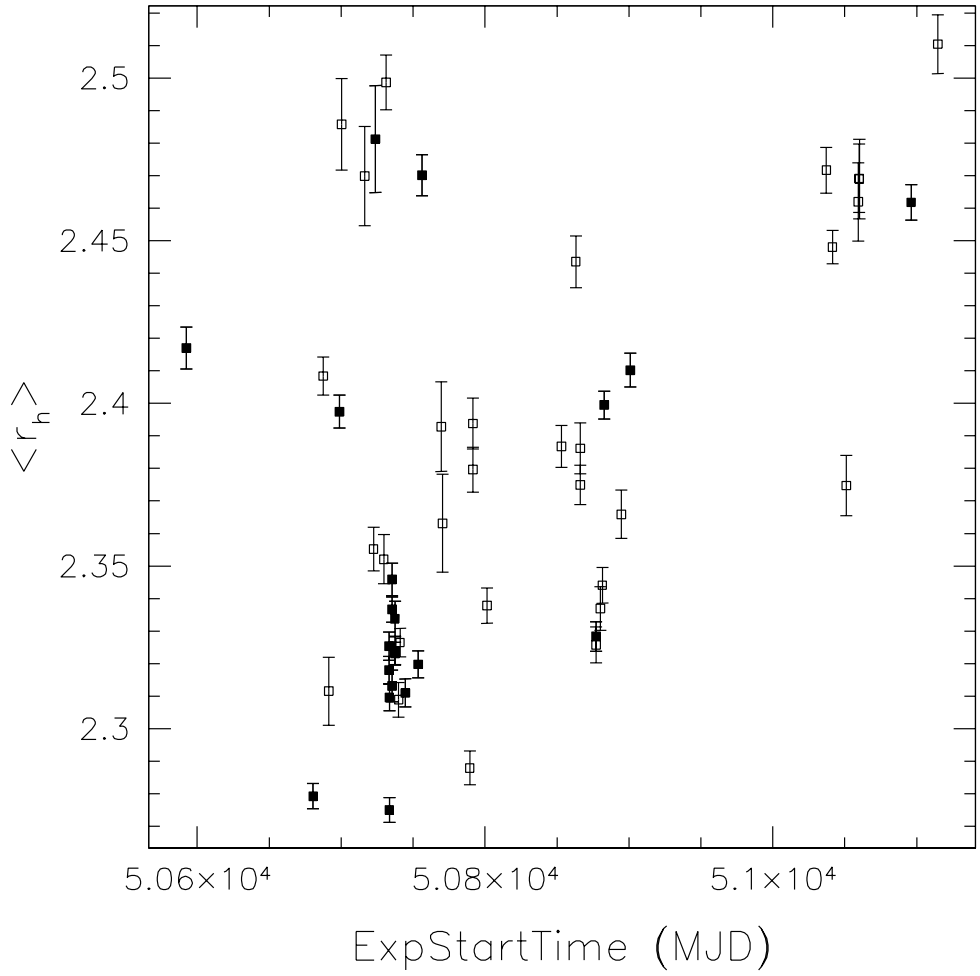

Fig. 10. The mean half-light radius of all stars in a star field vs. the time when the star field was observed. The filled squares represent those star fields which were selected for the anisotropy correction of the galaxy fields.

$\langle\overline{\gamma}^2\rangle = (-8.1 \pm 26.5) \times 10^{-4}$ for fields with $1 < N \leq 10$, $\langle\overline{\gamma}^2\rangle = (12.0 \pm 18.11) \times 10^{-4}$ for fields with $10 < N \leq 16$ and $\langle\overline{\gamma}^2\rangle = (23.4 \pm 14.0) \times 10^{-4}$ for fields with $N > 16$ when weighting individual galaxies with $w_{\rm NN}$ and galaxy fields with $W_{\rm f} = N$. This shows clearly that the cosmic shear estimate increases if we use fields with higher number density of galaxies. These fields have typically a larger exposure time and therefore probably probe higher redshifts. The main source for the better signal in these fields is the reduced error which is due to a better sampling of the intrinsic ellipticity distribution.

5.2. Effect of selection of galaxies and weighting

In the first three rows of Table 2 we present the results for the cosmic shear for different cuts in P^γ, weighting individual galaxies with $w_{\rm NN}$. If we lower the cut in P^γ, including galaxies whose high ellipticity is most probably only due to noise, we find that the cosmic shear estimator and the error increase.

In the second block of Table 2 we compare the cosmic shear estimator for weighting or not weighting individual galaxies. We find that the signal increases by one half for all bins if we apply weighting, whereas the error increases only slightly.

In the last block of Table 2 we give the values for our cosmic shear estimator applying different weights to the galaxy fields. We compare the results for applying no weighting at all, weighting by $W_{\rm f} = N$, which is the optimum weight if the error is only due to Poisson noise and weighting by $W_{\rm f} = N^2$. We do not discuss a weighting by exposure time, which would give deeper fields with a higher cosmic shear signal a larger weight, since our errors are mainly due to Poisson noise. Of course there is a strong correlation between exposure time and number density and therefore the weighting by N reflects the deepness of the fields, but there is also the effect of clustering. If we increase the weight of fields with many galaxies per field, the cosmic shear estimator increases if we take all fields, increases and then decreases if we take only fields with more than 10 galaxies and decreases if we take more than 15 galaxies per field. The error on the cosmic shear is the same for the $W_{\rm f} = 1$ and $W_{\rm f} = N$ weighting and is much larger for the $W_{\rm f} = N^2$ weighting. This weighting obviously gives a too large weight to fields with a very high number density of galaxies.

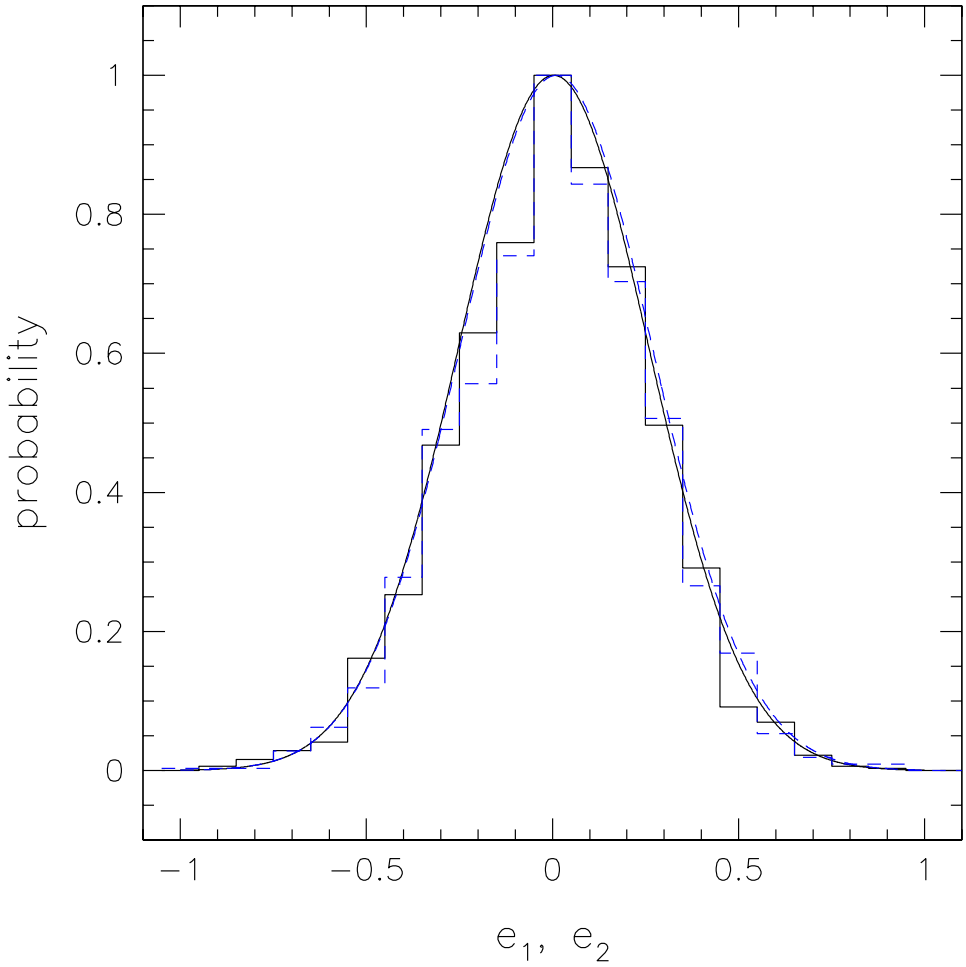

Fig. 11. Histogram of the probability distribution of the fully corrected ellipticities of all galaxies with $P^\gamma > 0.2$ in all fields, e_1 solid, e_2 dashed. The curves show Gaussians with mean and dispersion from the histograms. The mean ellipticity is very close to zero and $\sigma_1 = \sigma_2 = 26\%$.

5.3. Effect of PSF corrections

In order to estimate how much the PSF corrections affect our cosmic shear result we did the cosmic shear analysis without either anisotropy or smearing correction or both. The corresponding results are found in the first block of Table 3. Without the anisotropy correction but including the smearing correction ($e^{\rm raw}$, P^γ) the result does not change very much, which confirms that the STIS PSF anisotropy is sufficiently small. However, if we leave out the smearing correction ($e^{\rm ani}$, $P_{\rm sh}$ and $e^{\rm raw}$, $P_{\rm sh}$), we find that the cosmic shear estimator decreases by a factor of roughly three and also the dispersion is much smaller. This is not an effect of the different number of galaxy fields included in the averaging. The cosmic shear estimate is smaller because smearing tends to make objects rounder, and therefore any quantity calculated from the ellipticities is smaller. The dispersion decreases because P^γ is much noisier than $P_{\rm sh}$. In the last two rows of the first block of Table 3 we also give the results for the cosmic shear estimate if we apply *neither* PSF correction *nor* weighting. This demonstrates that the detection depends neither on the specific weighting scheme nor on the *necessary* smearing correction and can be seen in uncorrected data. However, in order to make an unbiased estimate of the shear dispersion, the PSF and smearing corrections must be taken into account and our particular choice of the weighting scheme minimizes the error on this estimate.

In the second block of Table 3 we show the cosmic shear estimator if we apply the PSF corrections from the star fields individually. Note that the number of galaxies per field (and therefore the number of fields with $N \geq N_{\rm min}$) also changes when correcting with different star fields, since the smearing correction $(P_{\rm sh}/P_{\rm sm})^*$ is different from star field to star field (as noted in Sect. 4.3). Therefore, for some galaxies P^γ is above or below the cut of 0.2 we introduced to reject objects with unphysically large ellipticities. Comparing the various results for the cosmic shear measurement, we find $\langle\overline{\gamma}^2\rangle = (16.0 \pm 1.2\ (\text{PSF}) \pm 11.8\ (\text{stat})) \times 10^{-4}$ for all fields, which shows that the difference between the star field corrections is much smaller than the statistical error.

In Fig. 14 we plot the mean cosmic shear estimators of the galaxy fields when correcting with different star fields vs. number of galaxies per field. As noted above, due to the cut in P^γ the number of galaxies per field can differ.

Table 2. Results for the cosmic shear estimator and errors for different minimum number of galaxies per field. N is the number of galaxies per field, $N_{\rm f}$ is the number of galaxy fields with $N \geq N_{\rm min}$. The first block shows the results for different cuts in P^γ, where we weight individual galaxies with $w = w_{\rm NN}$ and the galaxy fields with $W_{\rm f} = N$. In the next block the results are given for weighting individual galaxies or not. The last block shows the results for the cosmic shear if we apply different weights to galaxy fields, weighting them equally ($W_{\rm f} = 1$), weighting by the number of galaxies per field ($W_{\rm f} = N$) or by the square of the number of galaxies ($W_{\rm f} = N^2$). Note that we repeat the result with $P^\gamma > 0.2$, $w = w_{\rm NN}$, $W_{\rm f} = N$ in each block for easier comparison of the results.

	all			$N \geq 10$			$N \geq 15$		
	$N_{\rm f}$	$\langle\overline{\gamma}^2\rangle$ $\times 10^4$	$\sigma_{\langle\overline{\gamma}^2\rangle}$ $\times 10^4$	$N_{\rm f}$	$\langle\overline{\gamma}^2\rangle$ $\times 10^4$	$\sigma_{\langle\overline{\gamma}^2\rangle}$ $\times 10^4$	$N_{\rm f}$	$\langle\overline{\gamma}^2\rangle$ $\times 10^4$	$\sigma_{\langle\overline{\gamma}^2\rangle}$ $\times 10^4$
different cuts in P^γ; $w = w_{\rm NN}$; $W_{\rm f} = N$									
$P^\gamma > 0.2$	121	14.96	11.61	90	16.90	11.42	49	26.33	12.28
$P^\gamma > 0.1$	121	20.14	12.37	92	21.39	12.02	50	28.49	12.46
$P^\gamma > 0.0$	121	20.41	12.34	92	21.49	12.08	54	31.96	14.05
different weighting of individual galaxies; $P^\gamma > 0.2$; $W_{\rm f} = N$									
$w = 1$	121	9.18	10.17	90	10.29	10.05	49	19.03	10.68
$w = w_{\rm NN}$	121	14.96	11.61	90	16.90	11.42	49	26.33	12.28
different weighting of galaxy fields; $P^\gamma > 0.2$; $w = w_{\rm NN}$									
$W_{\rm f} = 1$	121	10.68	11.81	90	14.73	11.26	49	31.29	12.36
$W_{\rm f} = N$	121	14.96	11.61	90	16.90	11.42	49	26.33	12.28
$W_{\rm f} = N^2$	121	15.32	16.74	90	15.77	16.27	49	19.61	16.08

Table 3. Results for the cosmic shear for different PSF corrections. The first block shows the results if we do not correct for PSF effects: the first column indicates if we use raw ellipticities ($e^{\rm raw}$) or anisotropy corrected ellipticities ($e^{\rm ani}$) and if we apply the smearing correction (P^γ) or not ($P_{\rm sh}$). The first row gives the fully corrected result (see Table 2) for reference. The next block shows the results when we apply PSF corrections from the individual star fields. The results quoted were obtained weighting individual galaxies (see Eq. (9)) with $w = w_{\rm NN}$, requiring $P^\gamma > 0.2$ (or $P_{\rm sh} > 0.2$), and weighting the galaxy fields by $W_{\rm f} = N$ unless otherwise indicated.

e, P or starfield	all			$N \geq 10$			$N \geq 15$		
	$N_{\rm f}$	$\langle\overline{\gamma}^2\rangle$ $\times 10^4$	$\sigma_{\langle\overline{\gamma}^2\rangle}$ $\times 10^4$	$N_{\rm f}$	$\langle\overline{\gamma}^2\rangle$ $\times 10^4$	$\sigma_{\langle\overline{\gamma}^2\rangle}$ $\times 10^4$	$N_{\rm f}$	$\langle\overline{\gamma}^2\rangle$ $\times 10^4$	$\sigma_{\langle\overline{\gamma}^2\rangle}$ $\times 10^4$
$e^{\rm ani}$, P^γ	121	14.96	11.61	90	16.90	11.42	49	26.33	12.28
$e^{\rm raw}$, P^γ	121	16.14	11.73	90	18.25	11.52	49	27.61	12.43
$e^{\rm ani}$, $P_{\rm sh}$	121	5.27	6.00	101	5.33	6.04	67	10.33	6.58
$e^{\rm raw}$, $P_{\rm sh}$	121	5.69	6.02	101	5.75	6.06	67	10.87	6.58
$e^{\rm raw}$, $P_{\rm sh}$; $w = 1$; $W_{\rm f} = N$	121	4.63	4.49	101	4.80	4.50	67	8.72	4.68
$e^{\rm raw}$, $P_{\rm sh}$; $w = 1$; $W_{\rm f} = 1$	121	2.49	4.39	101	2.75	4.40	67	9.84	4.60
o3zf01_3	121	15.23	12.24	90	17.23	12.00	49	26.34	13.05
o46p1u_1	121	17.58	11.44	90	19.97	11.54	50	26.69	11.93
o46p4p_3	121	14.61	11.98	89	16.90	11.77	48	23.67	12.74
o48b3b_1	121	18.29	13.60	88	21.73	13.11	49	29.90	14.15
o48b3w_3	121	15.61	11.57	90	17.57	11.41	50	27.10	12.13
o48b3x_3	121	15.64	11.52	90	17.70	11.41	50	27.11	12.22
o48b41_3	121	15.93	11.50	90	18.01	11.40	50	26.98	12.12
o48b42_1	121	15.33	11.26	91	17.31	11.04	50	25.71	11.76
o48b45_3	121	16.02	11.51	90	18.15	11.39	50	27.49	12.21
o48b4j_3	121	15.35	11.38	90	17.37	11.27	50	26.67	12.06
o48b4k_3	121	15.79	11.50	90	17.93	11.41	50	27.36	12.26
o48b4v_1	121	18.07	11.52	91	20.55	11.57	50	27.04	12.13
o48b4w_1	121	15.36	11.28	90	17.38	11.17	50	25.98	11.86
o48b5j_3	121	15.30	11.38	90	17.28	11.25	50	26.69	12.04
o48b74_1	121	15.77	11.38	90	17.84	11.32	50	25.84	11.93
o48b8t_1	121	17.68	13.03	87	21.44	12.62	49	28.24	13.61
o48b9g_2	121	15.15	11.35	90	17.19	11.23	50	26.55	12.04
o4k1ez_1	121	14.76	12.10	89	16.95	11.84	48	23.85	12.74
o4lycf_1	121	15.05	11.40	90	16.99	11.26	50	26.31	12.02
o4lydt_1	121	16.20	12.39	90	18.27	12.15	49	27.94	13.12
o4xcll_1	121	18.21	12.97	87	21.93	12.52	49	28.43	13.45

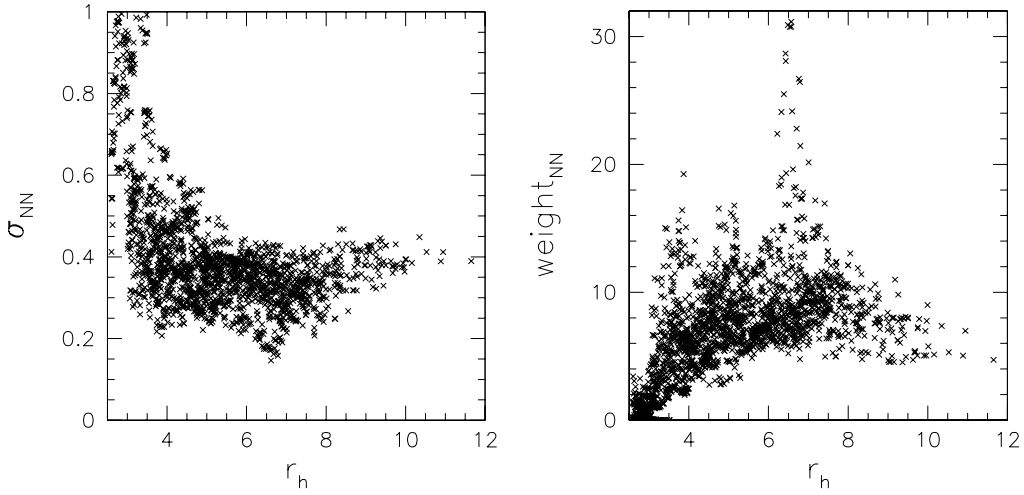

Fig. 12. In the left panel we show the dispersion $\sigma_{\rm NN}$ of individual galaxy ellipticities for the 20 next neighbours in the $r_{\rm h}$–S/N parameter space vs. half-light radius. In the right panel the weight deduced from this dispersion is shown.

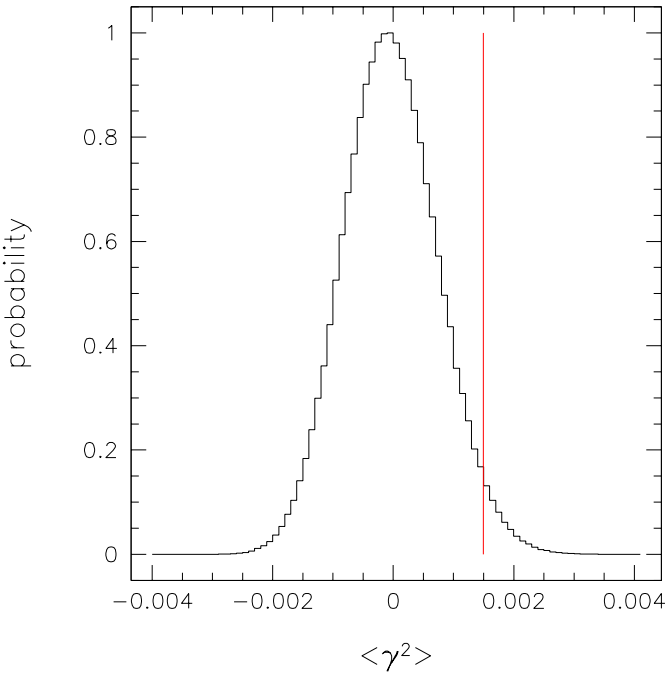

Fig. 13. Probability distribution of the cosmic shear estimator calculated from the data by randomizing the orientations of galaxies with $P^\gamma > 0.2$ in all galaxy fields. Individual galaxies are weighted with $w_{\rm NN}$ and the galaxy fields are weighted by the number of galaxies on each field. The vertical line indicates the actually measured value (see Table 2; 1st row).

The very large vertical error bars are due to different numbers of galaxies per field (including galaxies with high ellipticities or not). However, if we remove this effect by applying the cut on the mean P^γ over all star fields rather than the P^γ obtained from correcting with an individual star field, we still find variations of the cosmic shear estimator per galaxy field up to $\Delta\overline{\gamma}_n^2 = 0.004$, which is correlated with the mean shear per field. This can be understood by noting that

$$\overline{\gamma}_n^2 := \frac{1}{N_n(N_n-1)} \sum_{i\neq j} e_{in} e_{jn}^\star = \langle\gamma_n\rangle^2 - \frac{1}{N_n - 1}\,\sigma_{\rm s}^2; \quad (22)$$

then $\Delta\overline{\gamma}_n^2 = 2\,\langle\gamma_n\rangle\,\Delta\,\langle\gamma_n\rangle$. The spread in the cosmic shear values obtained from different fields decreases for larger N, which shows that fields with more galaxies are less affected by noise. Note that the cosmic shear estimator can also be negative.

5.4. Simulations

In order to test the analysis pipeline we produced 140 uncorrelated galaxy fields and 20 star fields ($1' \times 1'$).

Catalogues with intrinsic properties for the galaxies were produced with the `Stuff`[1] program (see Erben et al. 2001). The galaxies were taken to be at the same redshift ($z = 1$). The effect of cosmic shear was simulated by doing ray tracing through a number of lens planes which were produced from N-body simulations in an open CDM cosmology (Jain et al. 2000). Maps of the shear field produced from these simulations were sampled with randomly placed fields like the STIS fields. The cosmic shear signal on arcminute scales in these fields is $\sqrt{\langle\overline{\gamma}^2\rangle} = 2.6\%$ (Jain et al. 2000).

From the sheared galaxy catalogues, images were produced with `Skymaker`[1] (see Erben et al. 2001), where the parameters were tuned to match as closely as possible the physical characteristics of the STIS CCD for exposure times of 400 s, so noise properties of individual simulated images are very close to the ones observed in real data. Star fields were created directly using `Skymaker` in the stellar field mode. We focused on obtaining stars of similar

[1] Part of the Terapix software suite available at `http://terapix.iap.fr/soft/`

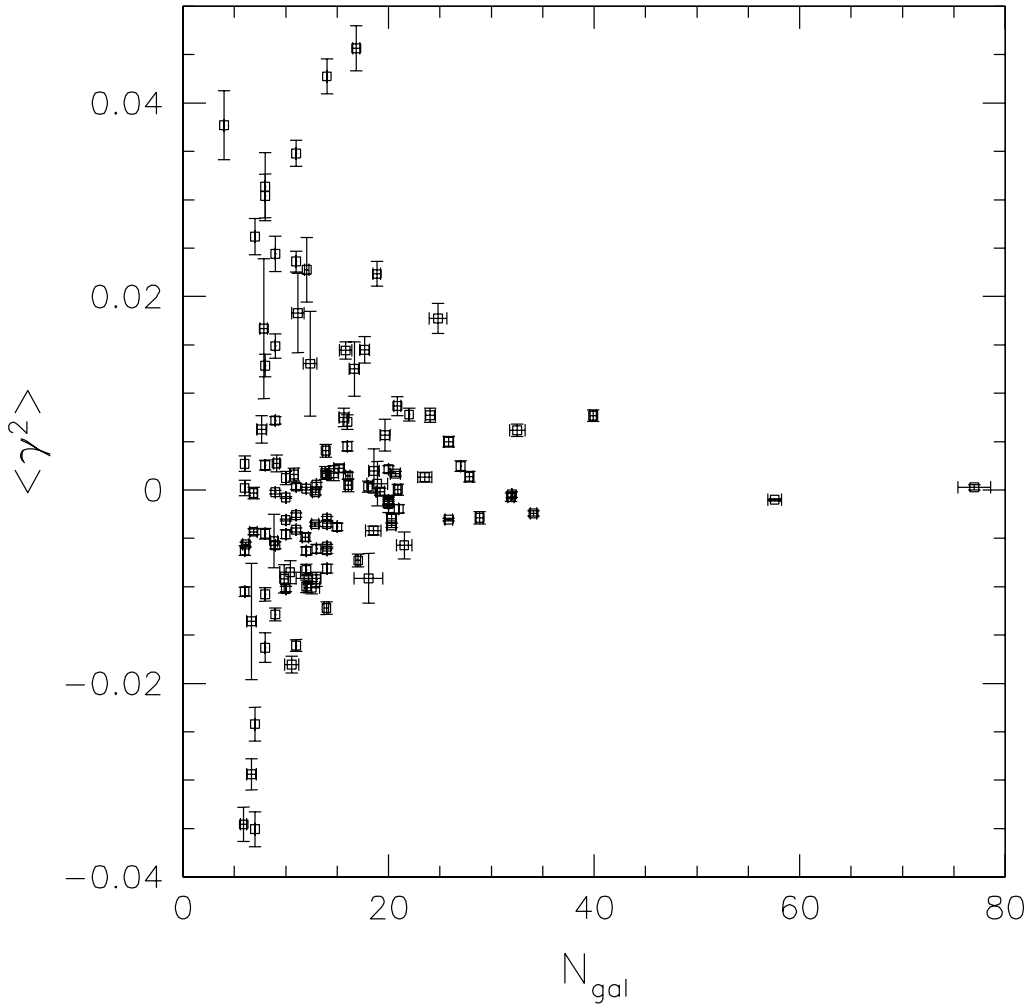

Fig. 14. For each of the 121 galaxy fields the cosmic shear was measured from ellipticities corrected with 21 individual star fields. We show the mean of the cosmic shear estimator over the star fields as boxes vs. the number of galaxies in the field. The error bars show the 1σ dispersion of individual values from the mean. Note that the number of galaxies per field can change because of the cut in P^γ.

half-light radii as the observed ones, by setting the tracking error type parameter in `Skymaker` to JITTER and its size to $0\farcs01$. We simulated a round PSF and did not try to include the effects of optical distortion of HST, since the simulations were just done to test the analysis pipeline and its capability to retrieve the input cosmic shear signal. To simulate a coadded exposure of 1600 s, we first created 4 individual 400 s images from the same original sheared galaxy catalogue, but with positions randomly dithered in order to process them in the same way as the real data. Dithers could vary between 0 and 30 pixels. The pipeline was able to recover the dithering within one tenth of a pixel as stated in Paper I. The images were then drizzled and median averaged in the same way as the archive data.

The analysis of the simulated fields was carried out following the same procedure for catalogue production and cosmic shear estimation as described in Sects. 2 and 5.1. In particular, we used the same parameters for simulated and real data. We find a cosmic shear signal of $\sqrt{\langle\overline{\gamma}^2\rangle} = 2.3\%$ with 1.6σ significance ($\langle\overline{\gamma}^2\rangle = (5.1 \pm 3.2) \times 10^{-4}$), which is slightly smaller than the input value of 2.6%. Since we under- rather than over-estimate the input signal we conclude that our procedure does not introduce a spurious cosmic shear signal.

For a quantitative analysis, we have to generate more realistic simulations which represent the properties of our data better with respect to different exposure times and therefore different redshift distributions, in order to better understand their contribution to the cosmic shear signal.

6. Discussion

We report on our initial measurement of cosmic shear on scales below one arcminute with STIS parallel archive data. Since any PSF anisotropy can mimic shear, we investigated the PSF anisotropy of the STIS CCD in detail. Although the STIS PSF is not stable in time, we show that the anisotropy on the STIS field is sufficiently small (on the order of 1%) to carry out the cosmic shear analysis. It changes the mean shear on galaxy fields by much less than 1% and does not affect our estimate of the cosmic shear

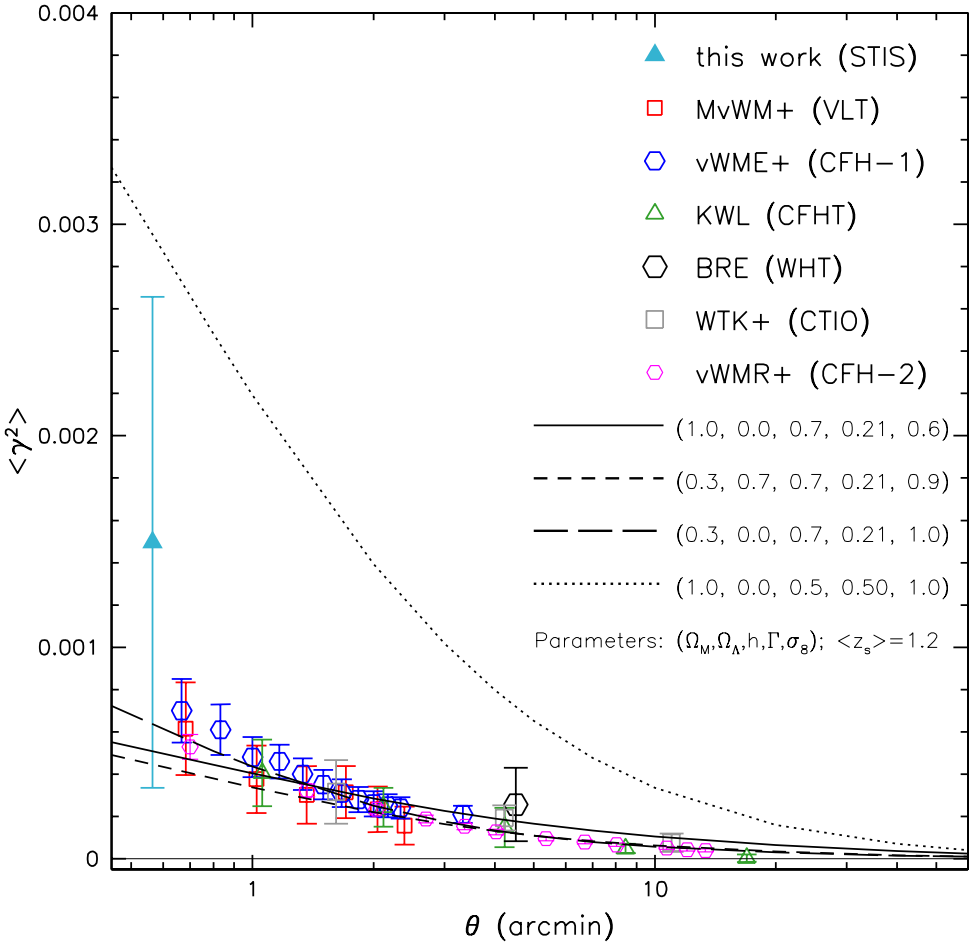

Fig. 15. Comparison of our cosmic shear result if we use all galaxy fields (weighting individual galaxies by $w_{\rm NN}$ and galaxy fields with N) with measurements at larger angular scales from other groups and with model predictions. θ is the radius in arcmin at which the results were obtained; the cosmic shear results which were measured on a square field (STIS, BRE, KWL) are plotted at the radius of a circular field with the same area, the result from WTK is plotted at half the separation angle of the galaxies. The lines show the theoretical predictions if one uses different cosmological models, which are characterized by $\Omega_{\rm m}$, Ω_Λ, h, Γ, and σ_8. The redshift distribution is taken from Brainerd et al. (1996), with a mean source redshift of $\langle z_{\rm s}\rangle = 1.2$.

rms by more than 10%. The smearing introduced by the PSF due to the small galaxy sizes at faint magnitudes is much more important than the PSF anisotropy and produces the biggest dispersion in our results. This is a rather fundamental problem in that the galaxies are small and only NGST will have a higher spatial resolution.

To test our procedure for catalogue production and cosmic shear estimation, we carried out simulations including the drizzling procedure. The cosmic shear result we obtained from the simulations is only slightly smaller than the input value, which shows that our procedure does not introduce a spurious cosmic shear signal and that our careful galaxy selection leads to a conservative estimation of the cosmic shear.

As discussed in Sect. 5.2 weighting of individual galaxies (according to the measurement error) or weighting of galaxy fields (to account for Poisson noise) changes the result substantially. If we restrict our analysis to fields with a higher number density of galaxies, we find that the signal increases on average, although not significantly. This would agree with a cosmological interpretation of the signal: fields with a higher number density of objects typically have a larger exposure time, therefore they typically probe higher redshifts and one expects a higher cosmic shear signal. For a quantitative interpretation of the cosmic shear measurement an optimal weighting scheme still has to be found, which will include redshift information on the STIS fields.

Although we obtained a detection of the cosmic shear the error bars are still large. As can be seen in Eqs. (12) and (13) the errors in the data depend on both the number of galaxies per field and on the number of fields. It is therefore important to get more fields with higher number densities of objects. The parallel observations with STIS are currently being continued in the frame of a GO cycle 9 parallel proposal (8562+9248, PI: P. Schneider).

In Fig. 15 we compare our result of $3.87^{+1.29}_{-2.04}\%$ for the cosmic shear to the ones obtained by other groups on larger scales and to the theoretically expected values when using different cosmological models with a mean redshift

of the sources of $\langle z_s \rangle \approx 1.2$, which is appropriate for the groundbased measurements. With the STIS data we are probably probing at higher mean redshifts, but since our observations with STIS were taken in the CLEAR filter mode, we do not have much information about the redshift range of our galaxies. Moreover, our fields have a large spread in exposure times and therefore we effectively average over different cosmic shear values. Multicolour (optical and near-IR) observations from the ground are presently being carried out to determine the redshift distribution of the galaxies in the STIS fields, using photometric redshifts on the actual observed STIS fields and their vicinity. With these data, we will be able to interpret the cosmic shear measurement with respect to other scales. This will be done in a forthcoming paper.

Acknowledgements. We thank Y. Mellier and L. van Waerbeke for fruitful discussions. We thank L. King and J. Sanner for careful reading of the manuscript. This work was supported by the TMR Network "Gravitational Lensing: New Constraints on Cosmology and the Distribution of Dark Matter" of the EC under contract No. ERBFMRX-CT97-0172 and by the German Ministry for Science and Education (BMBF) through the DLR under the project 50 OR106. RAEF is affiliated to the Space Science Department of the European Space Agency. BJ acknowledges funding support from STScI/NASA.

References

Bacon, D., Refregier, A., & Ellis, R. S. 2000, MNRAS, 318, 625 (BRE)
Bartelmann, M., & Schneider, P. 2001, Phys. Rep., 340, 291
Bernardeau, F., van Waerbeke, L., & Mellier, Y. 1997, A&A, 322, 1
Bertin, E., & Arnouts, S. 1996, A&AS, 117, 393
Blandford, R. D., Saust, A. B., Brainerd, T. G., & Villumsen, J. V. 1991, MNRAS, 251, 600
Bonnet, H., & Mellier, Y. 1995, A&A, 303, 331
Brainerd, T. G., Blandford, R. D., & Smail, I. 1996, ApJ, 466, 623
Erben, T., van Waerbeke, L., Bertin, E., Mellier, Y., & Schneider, P. 2001, A&A, 366, 717
Fruchter, A. S., & Hook, R. N. 2002, PASP, accepted [astro-ph/9808087]
Hoekstra, H., Franx, M., Kuijken, K., & Squires, G. 1998, ApJ, 504, 636
Hudson, M. J., Gwyn, S. D. J., Dahle, H., & Kaiser, N. 1998, ApJ, 503, 531
Jain, B., & Seljak, U. 1997, ApJ, 484, 560
Jain, B., Seljak, U., & White, S. 2000, ApJ, 530, 547
Kaiser, N. 1992, ApJ, 388, 272
Kaiser, N. 1998, ApJ, 498, 26
Kaiser, N., Squires, G., & Broadhurst, T. 1995, ApJ, 449, L105
Kaiser, N., Wilson, G., & Luppino, G. A. 2002, ApJ, submitted [astro-ph/0003338] (KWL)
Luppino, G. A., & Kaiser, N. 1997, ApJ, 475, 20
Maoli, R., van Waerbeke, L., Mellier, Y., et al. 2001, A&A, 368, 766 (MvWM)
Mellier, Y. 1999, ARA&A, 37, 127
Miralda-Escude, J. 1991, ApJ, 370, 1
Mould, J., Blandford, R., Villumsen, J., et al. 1994, MNRAS, 271, 31
Pirzkal, N., Collodel, L., Erben, T., et al. 2001, A&A, 375, 351 (Paper I)
Rhodes, J., Refregier, A., & Groth, E. J. 2001, ApJ, 552, L85
Schneider, P., van Waerbeke, L., Jain, B., & Kruse, G. 1998a, MNRAS, 296, 873
Schneider, P., van Waerbeke, L., Mellier, Y., et al. 1998b, A&A, 333, 767
van Waerbeke, L., Bernardeau, F., & Mellier, Y. 1999, A&A, 342, 15
van Waerbeke, L., Mellier, Y., Erben, T., et al. 2000, A&A, 358, 30 (vWME)
van Waerbeke, L., Mellier, Y., Radovich, M., et al. 2001, A&A, 374, 75 (vWMR)
Wittman, D. M., Tyson, J. A., Kirkman, D., Dell'Antonio, I., & Bernstein, G. 2000, Nature, 405, 143 (WTK)